

Optical phased array neural probes for beam-steering in brain tissue: supplement

WESLEY D. SACHER,^{1,2,3,*} FU-DER CHEN,^{2,3,†} HOMEIRA MORADI-CHAMEH,⁴ XINYU LIU,¹ ILAN FELTS ALMOG,² THOMAS LORDELLO,² MICHAEL CHANG,⁴ AZADEH NADERIAN,⁴ TREVOR M. FOWLER,¹ ERAN SEGEV,¹ TIANYUAN XUE,² SARA MAHALLATI,⁴ TAUFIK A. VALIANTE,^{4,5,6} LAURENT C. MOREAUX,¹ JOYCE K. S. POON,^{2,3} AND MICHAEL L. ROUKES¹

¹*Division of Physics, Mathematics, and Astronomy, California Institute of Technology, Pasadena, California 91125, USA*

²*Department of Electrical and Computer Engineering, University of Toronto, 10 King's College Rd., Toronto, Ontario M5S 3G4, Canada*

³*Max Planck Institute of Microstructure Physics, Weinberg 2, 06120, Halle, Germany*

⁴*Krembil Research Institute, Division of Clinical and Computational Neuroscience, University Health Network, Toronto, Ontario, Canada*

⁵*Division of Neurosurgery, Department of Surgery, Toronto Western Hospital, University of Toronto, Toronto, Ontario, Canada*

⁶*Institute of Biomaterials and Biomedical Engineering, University of Toronto, Toronto, Ontario, Canada*

*Corresponding author: wesley.sacher@mpi-halle.mpg.de

†These authors contributed equally to this work.

This supplement published with Optica Publishing Group on 18 February 2022 by The Authors under the terms of the [Creative Commons Attribution 4.0 License](https://creativecommons.org/licenses/by/4.0/) in the format provided by the authors and unedited. Further distribution of this work must maintain attribution to the author(s) and the published article's title, journal citation, and DOI.

Supplement DOI: <https://doi.org/10.6084/m9.figshare.17185418>

Parent Article DOI: <https://doi.org/10.1364/OL.441609>

Optical phased array neural probes for beam-steering in brain tissue: supplemental document

1. OPTICAL PHASED ARRAY BEAM PROFILE SIMULATIONS

We applied the beam propagation method (BPM) to simulate the optical scattering in tissue [1]. The model simulates the forward propagation of a beam in tissue with an iterative two-step process: 1) a two-dimensional phase mask is applied to the propagating beam, the phase mask has a small phase variance about the mean phase, which is equal to 0, and 2) beam propagation between the phase masks is assumed to only diffract, and it is modeled with the angular spectrum method [2]. The scalar electric field, E , is given by

$$E(k_x, k_y, z + d) = E(k_x, k_y, z) e^{in\sqrt{k^2 - k_x^2 - k_y^2}d}, \quad (S1)$$

where d is the propagation distance, n is the average refractive index of the medium, and k is the wavenumber (k_x and k_y are x and y components of the corresponding wavevector). The amplitude of any wave with $k_x^2 + k_y^2 > k^2$ is set to 0 as it is evanescent. The model is applicable to brain tissue since the beam is mostly forward scattered and its simulation results have been validated with the analytical solutions from the radiative transfer equation [1].

The patterns of the phase masks determine the scattering properties of the medium. We followed the design strategy in [1] to create the phase mask patterns. Each phase mask introduced a spatially varying random phase to the fields with the statistical properties governed by σ_p and σ_x . σ_p adjusted the variance of the phase introduced by each phase mask, which affected the scattering coefficient. Each phase mask was smoothed by a Gaussian filter with variance σ_x to control the phase correlation between pixels, which affected the anisotropy value. We also multiplied the beam profile with the attenuation factor after each propagation step. For the scattering simulation, we set the scattering coefficient (μ_s) to 200 cm^{-1} , the anisotropy of the tissue (g) to 0.83, and the attenuation coefficient (μ_a) to 0.62 cm^{-1} [3].

The field $3 \mu\text{m}$ above the optical phased array (OPA) was calculated and used as the launch field for the above propagation simulations. The SiO_2 cladding thickness above the OPA was $1 \mu\text{m}$. To calculate the launch field, the emission field from a single grating emitter array element of the OPA was first obtained ($3 \mu\text{m}$ above the grating) using finite difference time domain (FDTD) simulations, with the simulations performed for transverse magnetic (TM) polarized light in the waveguides. Then an array of single grating emitter field profiles was generated via laterally shifting the position of each subsequent emitter by the array pitch and applying phase shifts to each field profile corresponding to the wavelength and delay line parameters of the array element. Finally, the OPA field was the sum of the arrayed field profiles. This process was repeated for each simulated wavelength. The nominal OPA dimensions reported in the manuscript were used for the simulations. In addition, we corrected for the amplitude distribution across the output ports of the OPA star coupler by multiplying the emitter field profiles by an envelope function. We set the simulation domain volume to be $500 \mu\text{m} \times 500 \mu\text{m} \times 250 \mu\text{m}$ to avoid any edge effects while containing the entire simulation in the computer memory.

The same simulation model was used to study the OPA beam profiles in a non-scattering medium (water) with all phase masks set to a uniform value of 0. For verification, we compared cross-sections of beam profiles obtained from the BPM simulations and the conventional diffraction integral method. No significant differences were observed between the two methods at propagation distances of up to $200 \mu\text{m}$.

After the BPM simulations, we performed a series of steps to determine the 2D beam profile that would be expected from a top-down microscope as in the experimental apparatus in Fig. 1(e). First, we stacked the beam profile cross-sections to form a 3D model of the beam in tissue. We then rotated the model so that the beam propagation axis was parallel with the horizontal plane. Bicubic spline interpolation was used to interpolate the pixel values on the new grid of the rotated coordinate system. Lastly, a 2D beam profile was obtained by filtering and adding together the

transverse planes of the 3D beam profile model, i.e., all planes parallel to the microscope focal plane. To approximately emulate the microscope resolution limit, we applied a Gaussian filter to each transverse plane with filter size equal to the Gaussian propagation beam waist,

$$w(z) = w_0 \sqrt{1 + \left(\frac{\lambda z}{\pi w_0^2} \right)^2}, \quad (\text{S2})$$

where w_0 is the point spread function of the objective used in the experimental apparatus [Fig. 1(e)], and z is the distance of the transverse plane from the focal plane. For each simulation, the transverse plane with the highest intensity at the input to the scattering medium was selected as the focal plane.

The simulated and measured top-down beam profile FWHM values and peak-to-background ratios in Figs. 2, 3, and S2 were calculated along concentric arcs centered on the OPA emitting region; the radius of each arc was equal to the propagation distance. For the FWHM beam width calculations, the maximum was simply the maximum intensity along the arc, while for peak-to-background ratio calculations, to reduce the impact of noise, the peak intensity was defined as the average of the top 1% of intensity data points along the arc. The background intensity for the peak-to-background ratio calculations was defined as the intensity in the troughs between adjacent lobes. As the OPA beam profiles typically had 3 lobes (Figs. 2 - 3), the background intensity was calculated considering only the higher of the 2 troughs between the 3 lobes. The trough intensity was calculated as the average of the lowest 1% of intensity data points along the arc in the trough. The arcs spanned the central lobe and the two adjacent troughs.

2. EXPERIMENTAL APPARATUS

The scanning system in Fig. 1(a) is detailed in [4], with the exception that a wavelength-tunable laser was used here rather than a fixed wavelength laser. Briefly, light from the wavelength-tunable laser (TOPTICA Photonics Inc., DLC DL pro tunable laser system with integrated optical isolator, fiber coupler, motorized wavelength tuning, 484.3 - 491 nm wavelength tuning range) was coupled into a single-mode fiber (460-HP, Nufern Inc.), which was connected to an inline fiber polarization controller. The laser light was launched into free space using a fiber collimator, and this free-space laser beam was gated by a mechanical shutter, directed through a variable neutral density filter (for control of optical power), and input into the scanning system, as shown in Fig. 1(a). The scanning system included a 2-axis micro-electro-mechanical system (MEMS) mirror (A7B2.1-3600AL, Mirrorcle Technologies Inc.), two biconvex lenses with 35- and 150-mm focal lengths, and a $20\times$ objective lens (Plan Apochromat, 20-mm working distance, 0.42 numerical aperture, Mitutoyo Corporation). Actuation of the MEMS mirror enabled addressing of individual cores of the image fiber bundle (Fujikura FIGH-06-300S). The fiber bundle was optically coupled to and packaged together with the OPA neural probe using the method described in [4]. The packaged probe was attached to a 4-axis micro-manipulator (QUAD, Sutter Instrument Company) for immersing the probe in the fluorescein solution ($10 \mu\text{M}$ concentration, $\text{pH} > 9$) and inserting the probe into the brain slices. Since the OPA beam profiles were polarization-dependent, the fiber bundle was fixed in position during the experiments (to avoid polarization fluctuations due to movement of the fiber bundle). The input light to the neural probe chip was TM-polarized.

The maximum optical power available at the input to the scanning system was about 2 mW, and the loss of the scanning system (measured from the free-space input of the scanning system to the distal facet of the fiber bundle) was typically 40 - 60% (with the neutral density filter set to its minimum loss). The transmission of the OPA neural probe chip (from the facet of an optimally aligned single-mode fiber to the free-space OPA output) was typically about -20 dB. As described in [4], the edge couplers accounted for roughly 10 dB of this loss, and improved edge coupler designs may greatly improve the optical transmission of OPA neural probes. In addition, deviations of the fiber bundle core positions from a regular pitch and fiber misalignment during the optical packaging procedure resulted in significant variations in the coupling efficiency between the fiber bundle cores and the edge couplers of the neural probe. As a result, the total transmission of the OPAs (from the input to the scanning system to the free-space OPA output) varied from about -23 dB to -40 dB, with the majority of the OPAs having transmissions between about -23 to -33 dB.

The experimental apparatus used for OPA beam characterization and *in vitro* testing of the neural probe [Figs. 1(e) and 5(a)] included a Nikon Eclipse FN1 upright epifluorescence microscope

with an sCMOS camera (Zyla 4.2 PLUS, Andor Technology Ltd.) and a 10× objective lens (Plan Apochromat, 34-mm working distance, 0.28 numerical aperture, Mitutoyo Corporation). The images captured by the microscope were inverted (i.e., vertically mirrored). No image processing to correct the image inversion was applied, and the beam profile images [Figs. 2(a), 3(b), and 4(a)] and epifluorescence brain slice images [Figs. 5(b), 5(d), and S6(a)] are inverted. For the fluorescein and Thy1-GCaMP6s mouse brain slice imaging, an EGFP filter cube (49002, Chroma Technology Corporation) was used in the epifluorescence microscope, and for the VGAT-ChR2-EYFP mouse brain slice imaging, an EYFP filter cube (49003, Chroma Technology Corporation) was used. The camera exposure time was: 50 ms for the fluorescein beam profile images in Fig. 2(a), 500 ms for the *in vitro* brain slice beam profile images in Fig. 3(b), and 25 ms for the *in vitro* brain slice calcium imaging in Fig. 4. The microelectrode array (MEA) was a perforated design with 60 titanium nitride electrodes, 30 μm electrode diameter, and 100 μm electrode pitch (60pMEA 100/30iR-Ti-pr-6 mm high plastic ring, Multi-Channel Systems). MEA electrical activity recordings were performed using a MEA-1060-Up-BC amplifier and the MC Rack software (Multi-Channel Systems). The sampling rate for the MEA recordings was 25 kHz.

3. BRAIN SLICE PREPARATION

All experimental procedures described here were reviewed and approved by the animal care committees of the University Health Network in accordance with the guidelines of the Canadian Council on Animal Care. Brain slices were prepared from 40 - 80 days old VGAT-ChR2-EYFP (The Jackson Laboratory, stock number 014548) and Thy1-GCaMP6s (The Jackson Laboratory, stock number 025776) mice for the *in vitro* beam profile/optogenetic stimulation and the *in vitro* calcium imaging experiments, respectively; the brain slice preparation is detailed in [4]. 350 μm thick sagittal slices from the cerebellum were used for the *in vitro* beam profile and optogenetic stimulation experiments (Figs. 3 and 5, Visualization 2). A 300 – 450 μm thick horizontal slice from hippocampus was also tested during the beam profile experiments (Visualization 3), but the labeling was significantly more non-uniform compared to the slices from the cerebellum. The calcium imaging experiment used a 350 – 450 μm thick horizontal slice from the hippocampus. For the optogenetic stimulation and imaging experiments, brain slices were transferred to the MEA chamber, Figs. 1(e) and 5(a), and perfused with a constant flow of rodent artificial cerebrospinal fluid (ACSF) [5], which was continuously aerated with carbogen. During imaging of the Thy1-GCaMP6s mouse brain slice, KCl was added to the ACSF to increase the excitability of the neurons and the amount of spontaneous neuronal activity; the KCl concentration in the ACSF was 30 mM.

4. OPTOGENETIC STIMULATION PROTOCOL

For the single-OPA optogenetic stimulation experiment shown in Fig. 5(b,c), 10 optical pulses with a pulse width of 30 ms and a period of 200 ms were applied to the brain slice. A recovery period of 10 s was used after each stimulation pulse train. We repeated the pulse train 10 times.

For the multi-OPA optogenetic stimulation experiments shown in Figs. 5(e) and S6, multiple “stimulation trials” were performed, and for each trial, illumination was applied to the brain slice from one of the 4 OPAs in Figs. 5(d) and S6. Each trial corresponds to a point in Figs. 5(e) or S6, and the optical power was varied between trials. Each stimulation trial consisted of 3 sets of 10 optical pulses; the optical pulse width was 50 ms, the period was 200 ms, and the recovery period between each set of 10 optical pulses was 10 s. 7-8 trials with different optical power settings were performed for each OPA by using the variable neutral density filter in the experimental apparatus to reduce the input optical power to the scanning system in steps of approximately 10-20% of the maximum power. The trials were performed in the following order: 1) the optical power was set to the maximum value, 2) a trial was performed for each OPA sequentially (from OPA 1 to 4), 3) the optical power was reduced by a 10-20% increment, 4) the next set of OPA trials was performed. This process was repeated until 7-8 trials were performed for each OPA; at the lowest power setting, < 1 spike per optical pulse (on average) was observed. This procedure ensured that the stimulated electrical response caused by different OPAs could not have been simply due to variations in optical power between the OPAs. The recovery period between trials of the same optical input power but different OPAs was typically 20-60 s. The recovery period between trials where the input power was changed was 2 minutes and limited by the time required to adjust the variable neutral density filter.

5. SPIKE SORTING OF MICROELECTRODE ARRAY RECORDINGS

Spike sorting of the microelectrode array recordings was performed to analyze the data from the optogenetic stimulation (Figs. 5 and S6). The full electrical traces from each experiment, spanning all optical pulse trains and the recovery periods between them, were analyzed. We performed spike sorting with the Spyking Circus package [6]. We first selected the electrode channels where neuronal activity was detected in response to the optical stimulation. A bandpass filter with a passband from 300 to 3000 Hz was applied to the signal from each electrode channel. Then, any negative spike with amplitude larger than $6\times$ the mean absolute deviation was selected as a valid spike. Each spike waveform was extracted from a 3 ms time window centered at the spike peak. Then, to extract spike templates, a subset of 10000 spikes was selected; for data sets with < 10000 spikes, all spikes were selected. The selected spikes were projected to a lower dimension using Principal Component Analysis. We selected the first 5 prominent components as the basis. Then a density-based spike clustering algorithm was applied to cluster spikes with similar waveforms [6]. The median of the spike waveform in the same cluster was defined as the spike template of the cluster. Template matching was performed to decompose all spikes as a linear combination of the templates, addressing the problem of overlapping spikes [6]. Lastly, we performed a manual inspection of the sorted spikes in the phy GUI interface [7]. We selected the clusters that meet the following four criteria: 1) isolation distance > 10 , 2) likelihood ratio < 0.3 , 3) signal to noise ratio (SNR) > 2 [8–10], and 4) the percentage of spikes with interspike intervals < 2 ms was less than 2% when only considering the spikes in the optical stimulation windows. Only sorted spikes within an optical stimulation pulse window were accounted for in the spike rate calculations.

6. ADDITIONAL NOTES ON MICROELECTRODE ARRAY RECORDINGS

Figure S5 shows our analysis of the spike gain and spike latency for the optogenetic stimulation experiment in Fig. 5(d,e). We observed a long latency time between the start of each optical stimulation pulse and the first evoked spikes (>15 ms) and that spikes were evoked up to 300 - 400 μm away from the OPAs. These features suggest that most of the spikes we recorded were likely excited indirectly through synaptic connections to directly stimulated neurons [9] and that we were stimulating a network of neurons.

As our primary goal was to observe the change in spike rate with illumination patterns from the neural probe, expression of ChR2 in excitatory neurons (rather than inhibitory neurons as in the VGAT-ChR2-EYFP mice in this work) may have worked to our advantage. The baseline activity of the brain slices was low, and in our typical experiments, only $< 25\%$ of the channels recorded spikes. During optogenetic stimulation, we were likely stimulating a variety of interconnected inhibitory neurons in the cerebellar slices (including Purkinje cells, Golgi cells, Basket cells and Stellate cells). Stimulating inhibitory neurons can further suppress activity in connected neurons, which could have otherwise generated spikes in response to the optical stimulation. In addition, Purkinje cells and their synapses can span over 100 μm [11]. The dimensions of these cells is another possible reason why the experiment in Fig. 5(e) required switching between OPAs 250 μm apart to observe repeatable changes in the activity patterns on the MEA.

7. SUPPLEMENTARY FIGURES

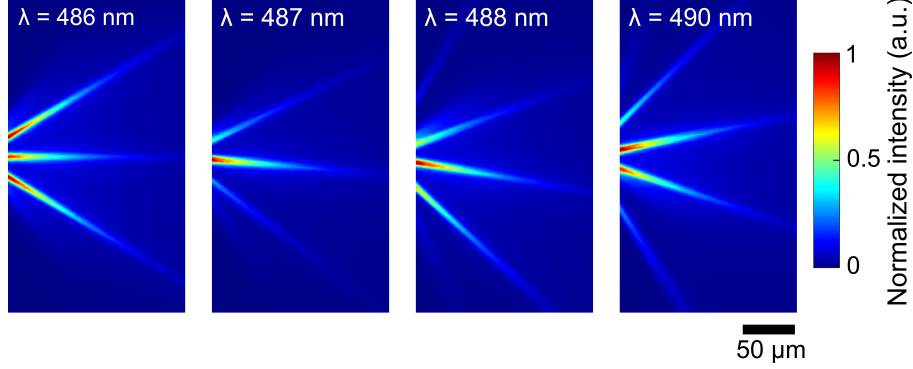


Fig. S1. Additional data for the OPA top-down beam profile simulations in brain tissue shown in Fig. 3(a). Here, the beam profiles from Fig. 3(a) have been cropped by $30 \mu\text{m}$ on the left side (closest to the OPA). The visibility of the beam profiles is improved since the large beam intensity at the OPA emitter is removed and each intensity color scale is normalized to the maximum of the lobes after they have separated.

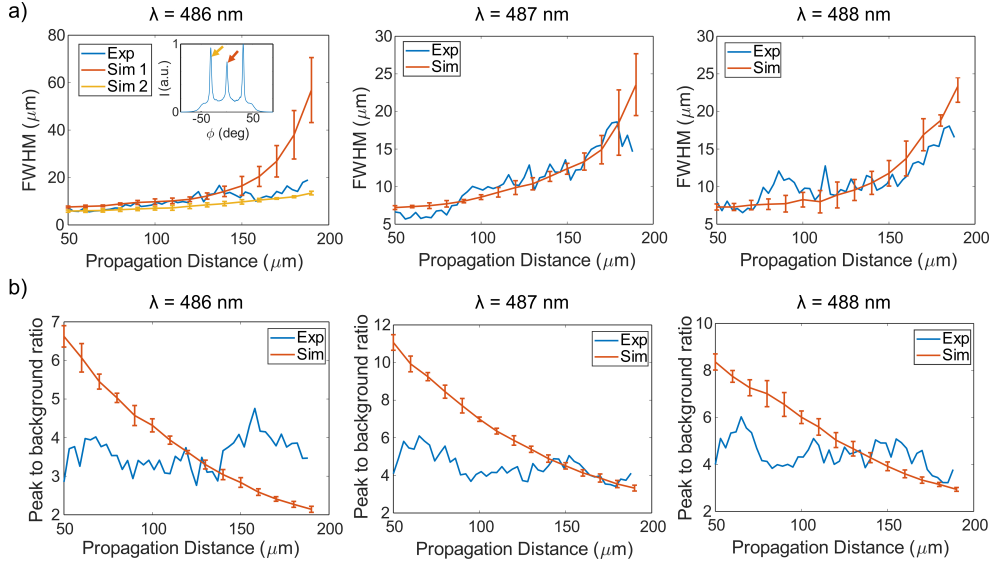


Fig. S2. Additional data for the OPA top-down beam profile simulations and measurements shown in Fig. 3. Simulated and measured intensity beam profile characteristics are shown at wavelengths of 486, 487 and 488 nm. (a) Measured and simulated FWHM beam width versus propagation distance. (b) Measured and simulated ratios of peak beam intensity to background intensity versus propagation distance. Each data point for the simulated beam profiles from (a) and (b) is an average over 5 simulations with different random phase masks. The bars represent the standard deviation of the 5 simulations at each propagation distance. The FWHM plot for $\lambda = 486 \text{ nm}$ shows 2 simulations: "Sim 1" is the simulated FWHM of the central lobe emitted by the OPA, and "Sim 2" is the FWHM of a side lobe. The inset shows the simulated intensity (I) profile from Fig. 3(a) (propagation distance = $100 \mu\text{m}$, $\lambda = 486 \text{ nm}$) with arrows indicating the lobes corresponding to "Sim 1" and "Sim 2". The central lobe is less intense than the side lobes at this wavelength, a result of the non-uniformity of the emissions of the individual gratings in the OPA versus steering angle ϕ , i.e., the envelope of the emitters. Consequently, for propagation distances beyond $\approx 120 \mu\text{m}$, the background intensity contributes more significantly to the FWHM of the central lobe than the side lobes, leading to a large FWHM for "Sim 1" relative to "Sim 2" and $\lambda = 487$ and 488 nm .

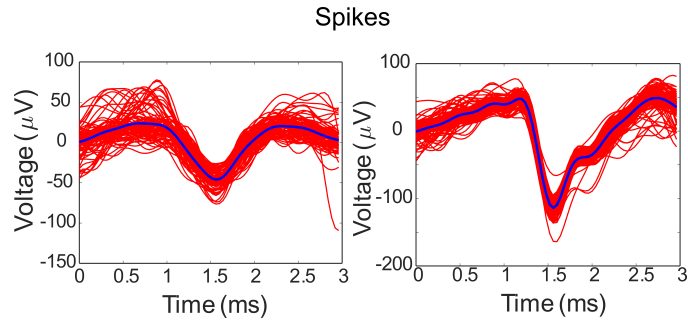


Fig. S3. Additional data for the optogenetic stimulation experiment in Fig. 5(b,c). Examples of sorted spikes from Channel (“Chn”) 42 of the MEA. The spikes were recorded during optical stimulation.

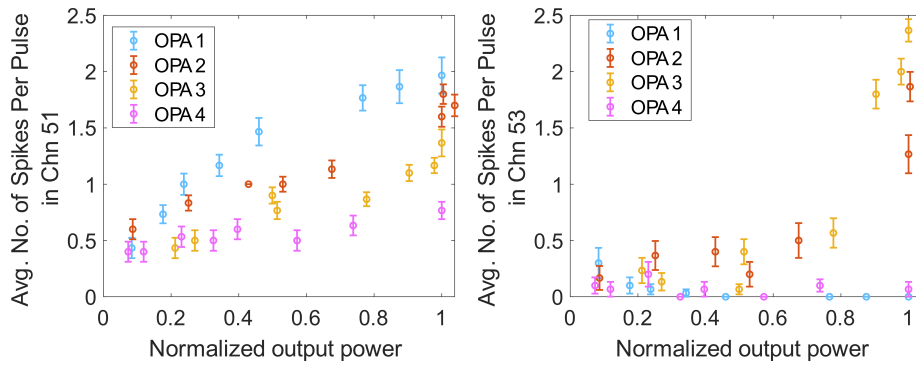


Fig. S4. Additional data for the optogenetic stimulation experiment in Fig. 5(d,e). Dependence of the average number of spikes per optical stimulation pulse (recorded by MEA Chn 51 and 53) on the optical power emitted by the four OPAs. The optical power was normalized to the initial power emitted by each OPA, which was estimated to be $\sim 5 \mu W$ for OPAs 1 - 4. In the experiment, we decreased the power in increments of 10-20% of the initial power until the power was around 10% of its initial value.

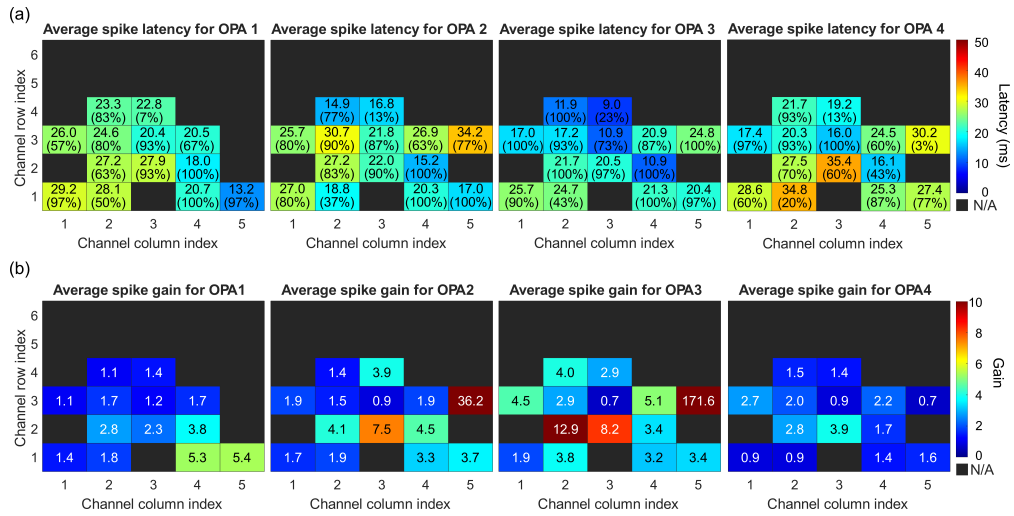


Fig. S5. Additional data for the optogenetic stimulation experiment in Fig. 5(d,e). (a) Average spike latency across MEA Chn 11 to Chn 56 in response to the 30 optical stimulation pulses from the first power setting (typically the maximum power) of the 4 OPAs. The value in parentheses is the percentage of optical pulses that contained at least one spike. Spike latency is the time difference between the onset of the first spike evoked within the stimulation pulse and the rising edge of the optical pulse. The blank entries indicate electrodes with no spikes within all 30 stimulation pulses. (b) Average spike gain across MEA Chn 11 to Chn 56 in response to the 30 optical stimulation from the first power setting of the 4 OPAs. Spike gain is defined as the ratio between the spike rate during each optical stimulation pulse and the spike rate within a time window of 20 to 5 seconds before the start of each OPA trial. The x and y axes in (a) and (b) indicate the index position of the electrode channel (i.e., Chn 53: Channel column index = 5, Channel row index = 3). No response to optical stimulation was observed on the remaining electrodes of the MEA, Chn 61 to 106, not shown here.

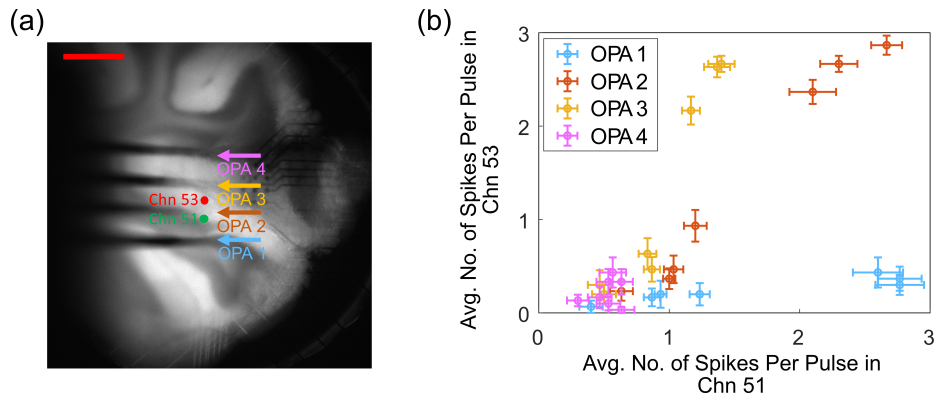


Fig. S6. Additional optogenetic stimulation experiment showing the stimulation effects of 4 of the neural probe OPAs on an *in vitro* brain slice. The experiment was performed on a 350 μm thick sagittal cerebellar slice obtained from a VGAT-ChR2-EYFP mouse; the same brain slice as in Figs. 5(d) and (e). The fluorescence image (a) shows the relative positions of the OPAs with respect to the MEA channels of interest; epi-illumination from the top-down microscope was applied for visibility of the shanks and the structure of the brain slice. (a) is repeated from Fig. 5(d). The scale bar is 500 μm . (b) shows the average number of spikes per optical pulse from 4 of the OPAs on two different MEA channels ("Chn"). As in Fig. 5(e), each point in (b) is from one stimulation trial consisting of 3 sets of 10 optical pulses; the optical pulse width was 50 ms, the period was 200 ms, and the recovery period between each set of 10 optical pulses was 10 s. The optical power was reduced across the trials for each OPA. The error bars represent the standard error of the mean number of spikes per pulse in a trial.

REFERENCES

1. X. Cheng, Y. Li, J. Mertz, S. Sakadžić, A. Devor, D. A. Boas, and L. Tian, "Development of a beam propagation method to simulate the point spread function degradation in scattering media," *Opt. Lett.* **44**, 4989–4992 (2019).
2. J. W. Goodman, *Introduction to Fourier optics* (Roberts and Company Publishers, 2005).
3. G. Yona, N. Meitav, I. Kahn, and S. Shoham, "Realistic numerical and analytical modeling of light scattering in brain tissue for optogenetic applications," *eNeuro* **3** (2016).
4. W. D. Sacher, F.-D. Chen, H. Moradi-Chameh, X. Luo, A. Fomenko, P. Shah, T. Lordello, X. Liu, I. Felts Almog, J. N. Straguzzi, T. M. Fowler, Y. Jung, T. Hu, J. Jeong, A. M. Lozano, P. G.-Q. Lo, T. A. Valiante, L. C. Moreaux, J. K. S. Poon, and M. L. Roukes, "Implantable photonic neural probes for light-sheet fluorescence brain imaging," *Neurophotonics* **8**, 025003 (2021).
5. J. T. Ting, B. Kalmbach, P. Chong, R. de Frates, C. D. Keene, R. P. Gwinn, C. Cobbs, A. L. Ko, J. G. Ojemann, R. G. Ellenbogen, C. Koch, and E. Lein, "A robust ex vivo experimental platform for molecular-genetic dissection of adult human neocortical cell types and circuits," *Sci. Reports* **8**, 8407 (2018).
6. P. Yger, G. L. Spampinato, E. Esposito, B. Lefebvre, S. Deny, C. Gardella, M. Stimberg, F. Jetter, G. Zeck, S. Picaud *et al.*, "A spike sorting toolbox for up to thousands of electrodes validated with ground truth recordings in vitro and in vivo," *eLife* **7**, e34518 (2018).
7. C. Rossant, A. Buccino, M. Economo, C. Gestes, D. Goodman, M. Hunter, S. Kadir, C. Nolan, M. Spacek, and N. Steinmetz, "phy: interactive visualization and manual spike sorting of large-scale ephys data," <https://github.com/cortex-lab/phy> (2020).
8. N. Schmitzer-Torbert, J. Jackson, D. Henze, K. Harris, and A. Redish, "Quantitative measures of cluster quality for use in extracellular recordings," *Neuroscience* **131**, 1–11 (2005).
9. S. Libbrecht, L. Hoffman, M. Welkenhuysen, C. Van den Haute, V. Baekelandt, D. Braeken, and S. Haesler, "Proximal and distal modulation of neural activity by spatially confined optogenetic activation with an integrated high-density optoelectrode," *J. Neurophysiol.* **120**, 149–161 (2018).
10. U. Rutishauser, E. M. Schuman, and A. N. Mamelak, "Online detection and sorting of extracellularly recorded action potentials in human medial temporal lobe recordings, in vivo," *J. Neurosci. Methods* **154**, 204–224 (2006).
11. B. Asrican, G. J. Augustine, K. Berglund, S. Chen, N. Chow, K. Deisseroth, G. Feng, B. Gloss, R. Hira, C. Hoffmann, H. Kasai, M. Katarya, J. Kim, J. Kudolo, L. Lee, S. Q. Lo, J. Mancuso, M. Matsuzaki, R. Nakajima, Li. Qui, G. Tan, Y. Tang, J. T. Ting, S. Tsuda, L. Wen, X. Zhang, and S. Zhao "Next-generation transgenic mice for optogenetic analysis of neural circuits," *Front. Neural Circuits* **7**, 160 (2013).